Punching Shear Behavior and Corrosion Resistance of Composite Slab-Column Connections using Hybrid BFRP and Steel Rebar Reinforcement

Kai Qian[1*], M. ASCE, Yun-Hao Weng[2]., Shi-Lin Liang[3], Feng Fu, F. ASCE [4]

Abstract

The collapse of Champlain Towers in South, Miami in 2021 shows that flat slab structures in coastal region show high risk of building collapse due to rebar corrosion. However, to date, few studies have been carried out to avoid these types of tragic events. A new type of hybrid steel bars and basalt fiber reinforced polymer (BFRP) bars reinforcement will provide a possible solution due to their excellent erosion resistance features. Thus, in this study, an experimental study of eight large-scale composite slab-column connections is conducted to investigate the advantages of partially replacing steel bars using equal-stiffness BFRP bars to resist corrosion. Two normal reinforced concrete (RC) slab-column connections were first tested as reference specimens, together with two corroded counterparts having a target corrosion degree of 20%. Then, two composite connections with hybrid rebars were tested to investigate the advantage of replacing half of the steel bars with BFRP bars based on equal-stiffness rule. Finally, two composite connections were reinforced by hybrid rebar and the steel rebar was corroded with a target corrosion degree of 20% to investigate the effectiveness of hybrid reinforcement to compensate the decrease in punching shear resistance due to corrosion. The test results demonstrated that the RC slab-column connections with tensile reinforcement ratio of 0.52% and 0.91% reduced the punching shear resistance by 19.7% to 24.3% when the real corrosion degree reached 12.8% and 18.9%, respectively. Replacement of steel rebar with BFRP bar following equal-stiffness rule resulted in slightly greater load resistance but lower ductility energy dissipation capacity. The punching shear resistance of the corroded composite slab-column connections with hybrid bars was greater than that of the corroded conventional RC slab-column connections. To incorporate the rebar corrosion effects in design, the accuracy of the equations from prevalent design codes was re-evaluated, design recommendation was made.

Author keywords: Punching shear failure; Slab-column connection; Corrosion; Large-scale test; BFRP bars

[1]Professor, Guangxi Key Laboratory of Green Building Materials and Construction Industrialization, Guilin University of Technology, Guilin, 541004, China. qiankai@glut.edu.cn

[2]Research Fellow, Guangxi Key Laboratory of Green Building Materials and Construction Industrialization, Guilin University of Technology, Guilin, 541004, China. wengyunhao@glut.edu.cn

[3] Ph.D. Candidate, College of Civil and Transportation Engineering, Hohai Univ., Nanjing 210098, China. Email: liangshilin@st.gxu.edu.cn

[4] Senior Lecturer (Associate Professor) in Structural Engineering, Department of Engineering, School of Science and Technology, City, University of London, U.K., Feng.Fu.1@city.ac.uk, Adjunct Professor, Guilin University of Technology. corresponding author: Feng.Fu.1@city.ac.uk

Introduction

Flat slab/plate system is widely used in parking garages, office, and residential buildings because the absence of down stand beams enables a clear story height and efficient space usage. The failure of flat slab/plate system may be due to punching shear failure at the slab-column connections, which is quite dangerous due to its brittle failure nature. Once a punching shear failure occurs at one of the connections, the force initially resisted by the column required to redistributed to surrounding connections and resulted in greater bending moment and shear force at these connection. Finally, the punching shear failure may also occur at these surrounding connections, which leads to a progressive collapse of the whole building (Weng et al. 2020). As flat slab/plate is normally built as basement, parking lot or servicing in coastal environment are exposed to moisture, chlorides, and dry-wet cycles. In this context, steel bar corrosion is one of the major concerns that may lead to building collapse, such as the collapse of the Champlain Towers South, Miami in 2021 and partial collapse of Pipers Row car park, Wolverhampton, UK in 1997. Corrosion deteriorates steel bar and concrete, as well as the bond between steel bar and concrete, thereby impairing the stiffness and strength of structural members (Cairns et al. 2005). When the corrosion degree is greater than 2%, the decrease in bond strength, stiffness, and slip is considerable, which can cause a brittle failure (Auyeung et al. 2000). Therefore, it is necessary to explore the adverse effects of rebar corrosion on the punching shear resistance of slab-column connections.

To date, few tests have been conducted to investigate the effects of corrosion on structural performance of slab-column connections or two-way slabs. Said and Hussein (2019a and b) studied the performance of two-way slabs with corrosion degrees of 0%, 15%, 25%, and 50% and concluded that the increasing corrosion degree resulted in a decrease in the punching shear resistance and initial stiffness although the energy-absorption capacity and ductility were increased. Qian et al. (2022a and b) investigated the slab-column connections with target corrosion degree of 10%, 20%, and 30% and demonstrated that, compared with uncorroded slab-column connections, the failure mode of the corroded slab-column connections might be changed from flexural or flexural-shear failure to punching shear failure. Moreover, the horizontal cracks caused by corrosion significantly decreased the initial stiffness and punching shear resistance of the connections. On the basis of a critical shear crack theory (Muttoni 2008), a modified model taking into account the corrosion effects was proposed by Qian et al. (2022a).

To mitigate the detrimental influences of corrosion, corrosion-resistant fiber reinforced polymer (FRP) bars were used to replace steel bars of slab-column connections (Hassan et al. 2013a and b; Long and Marián 2013; Aljazaeri et al. 2020; Huang et al. 2020; Sim and Frosch 2020). However, these studies replaced all steel bars by FRP bars completely based on equal area rule. It is predictable that, if the steel bars were completely replaced by FRP bars relied on equal area rule, the slab-column connections may perform poorly than conventional RC slab-column connections because of the lower elastic modulus of FRP bars (Hassan et al. 2013a and b; Long and Marián 2013). Therefore, to achieve similar stiffness and load resistance, the equal-stiffness replacement rule was adopted in the current study. However, because of the low elastic modulus of basalt fiber reinforced polymer (BFRP) bars, the area of BFRP bars should be several times than that of steel bars to achieve similar stiffness, which significantly increases reinforcement ratio, resulting in construction congestion and additional costs. Thus, compared with the complete replacement scheme, partial replacement based on equal-stiffness rule is more practical. However, to date, little relevant study was reported. In this study, eight large-scale composite slab-column connections were tested to investigate the efficiency of proposed partial replacement rule and corrosion effects. It should be noted that glass fiber reinforced polymer (GFRP) bars were not used as their lower stiffness and strength while carbon fiber reinforced polymer (CFRP) bars were not used as their much higher cost. BFRP bars were used in this study due to their relatively high stiffness and strength, but much lower cost.

Experimental Study

Specimen and Material Properties

Fig. 1 shows the geometry and reinforcing details of the specimens. The slab was 150 mm in thickness and 2,200 mm in both length and width. The cross section of the column stub was 200 mm × 200 mm. Based on the slab reinforcement ratio, the test specimens were categorized into L- and H-series, as listed in

Table 1. The first letter, L or H indicates low or high reinforcement ratio of 0.52% and 0.91%, respectively. Each series included four specimens, the numeral in the specimen notation represents corrosion degree. The second letter *S* denotes the specimens with equal-stiffness replacement. As illustrated in **Fig. 1**, in Specimens L-S-0, L-S-21.1, H-S-0, and H-S-22.2, half of the steel bars in the zone highlighted by the red dashed lines were replaced by BFRP bars following equal-stiffness rule. The area of BFRP bars A_b was determined by **Eq. 1** and the equivalent reinforcement ratio of the hybrid steel and BFRP bars ρ_b was calculated by **Eq. 2**. For Specimens L-12.8, L-S-21.1, H-18.9, and H-S-22.2, the steel bars within the corrosion zone (hatched zone) were corroded to the target corrosion degree of 20% by electrified accelerated corrosion. The dimension of the corroded zone, 800 mm × 800 mm, was designed to ensure the critical shear crack (if any) to be within the corroded zone. The bottom steel bars of the slab were designed as T10@260 for all specimens. T10 indicates a deformed steel bar with a 10-mm nominal diameter. Based on uniaxial compression tests and splitting tests, the compressive and tensile strength of concrete cylinders is shown in

Table 1**.** The material properties of the steel and BFRP bars are listed in **Table 2** and shown in **Fig. 2**.

$$A_{\mathrm{b}} = \frac{E_{\mathrm{s}}}{E_{\mathrm{b}}} A_{\mathrm{s}} \tag{1}$$

$$\rho_{\mathrm{h}} = \rho_{\mathrm{b}} \frac{E_{\mathrm{b}}}{E_{\mathrm{s}}} + \rho_{\mathrm{s}} \tag{2}$$

Accelerated Corrosion

Fig. 3 shows the device for electrified accelerated corrosion. A temporary tank was fabricated on the bottom surface of the specimens (top surface in actual constructions), which contained 5% electrolyte NaCl solution. A stainless steel gauze immersed in the solution and the steel bars within the target zone were connected to the cathode and anode of a direct current (DC) power source, respectively. The impressed constant current density was 0.6 mA/cm^2. Based on **Eq. 3**, the required corroding time to achieve the target corrosion degree of 20% was 34 days.

$$t = \frac{zFm}{MI} \tag{3}$$

where t is corroded time (in s); m is mass of corroded steel bars (in g); M is atomic weight of the steel equal to 56g; I is current amperes (in A); z is ionic charge (2 for $Fe \rightarrow Fe^{2+}$ +2e-); and F is Faraday’s constant equal to 96,500 A/s.

Test Setup and Instrumentation

Fig. 4 shows the test setup. The specimens were simply supported along four edges. A concentrated load was applied to the top of the column stub by a hydraulic jack with a loading capacity of 2,000 kN. Displacement-control loading scheme was implemented. A load cell was installed below the hydraulic jack to measure the applied load. As shown in **Fig. 5**, six linear variable differential transformers (LVDTs) were installed to measure slab deflections. Moreover, strain gauges were installed to the steel bars of uncorroded specimens. Test data were collected at a sampling frequency of 5 Hz during the entire loading process.

Test Results and Discussions

Corrosion Measurement

As shown in **Fig. 6**, the corroded zone was divided into four regions according to the distance of their outer boundaries to the column center at an interval of 100 mm. After testing, four 400-mm-long steel bars, oriented in the four different directions, were extracted. In other words, a total of 16 samples were collected from each corroded specimen. Each bar was then cut into four 100 mm-long pieces, each corresponding to a corroded region. The corrosion degree *w* for each piece was then determined in accordance with **Eq. 4**. As shown in **Fig. 6**, the measured *w* in the four regions of L-12.8 and H-18.9 were generally lower than the target value. This might be because the current loss owing to the unavoidable solution leakage from the bottom of the tank. However, the measured *w* of L-S-21.1 and H-S-22.2 was close to the target one. Finally, the average *w* over regions 2 and 3 was used to represent the corrosion degree of the specimens because punching shear failure was expected to occur in these two regions. As listed in

Table 1. the corrosion degrees of L-12.8, H-18.9, L-S-21.1, and H-S-22.2 determined in this manner were 12.8%, 18.9%, 21.1%, and 22.2%, respectively.

$$w = \frac{W_0 - W}{W_0} \times 100\ (\%) \tag{4}$$

where W_0 and W are the masses of a steel rebar before and after the corrosion, respectively.

Crack Pattern and Failure Mode

Fig. 7 shows the crack pattern and failure mode of the specimens viewed from slab bottom (tension face). For corroded specimens, due to corrosion expansion, initial cracks along the corroded steel bars were observed before testing. The initial cracks widened when the applied load reached about 30% of the ultimate load given in **Table 3**. For the uncorroded specimens, the first crack occurred at approximately 35% of the ultimate load. These cracks extended to the edges of the specimens with increasing load. In the final, the critical shear crack and circumferential cracks widened and resulted in the sudden drop in load resistance. The measured radius of concrete cover spalling R_s, which is defined as the average radius measured in the bottom surface of a specimen, is summarized in **Table 3** and shown in **Fig. 7**. In general, the R_s of corroded specimens was larger than that of the corresponding uncorroded specimens, which could be attributed to the initial horizontal cracks along the steel bars. After testing, the specimens reinforced with hybrid bars were vertically cut along a column face to expose the inclined shear cracks that caused the failure. As shown in **Fig. 8**, for the uncorroded Specimens L-S-0 and H-S-0, the diagonal cracks penetrated the whole slab thickness directly. Differently, for corroded specimens L-S-21.1 and H-S-22.2, the diagonal cracks penetrated the effective slab thickness and intersected with the initial horizontal cracks, and then developed along the horizontal cracks. The formation of the horizontal cracks was mainly attributed to the corrosion-induced radial expansive stress of the steel bars (Weng et al. 2023). The radius of the punching shear core, which is defined as the distance from the intersections of the inclined cracks and the tension rebars to the column center, of L-S-0, H-S-0, L-S-21.1, and H-S-22.2 observed in **Fig. 8** was about 275 mm, 500 mm, 412 mm, and 525 mm, respectively. The radius increased with increasing reinforcement ratio. In theory, the radius should be decreased when the rebars were corroded, however, vice versa was observed in **Fig. 8**. This may be attributed to randomness in tests because the specimens were only cut along one column face.

Fig. 9 shows the response of crack width vs applied load. In general, the crack width increased linearly with the applied loads. Initial cracks were found in the slabs of the corroded specimens after corrosion and removal of corrosion products. The initial crack width of L-12.8, L-S-21.1, H-18.9, and H-S-22.2 was 0.12 mm, 0.13 mm, 0.13 mm, and 0.10 mm, respectively. The cracks of the corroded specimens were wider than those of the uncorroded specimens under the same applied load.

Load-Displacement Curves

Fig. 10 shows the load-displacement response of the specimens. The critical values are summarized in **Table 3**. Comparing **Fig. 10** (a) and (b) found that the specimens with a tension reinforcement ratio of 0.91% achieved much higher initial stiffness than those with a tension reinforcement ratio of 0.52%. Decreasing the tension reinforcement ratio from 0.91% to 0.52% led to a 25.5% decrease in the punching shear resistance for uncorroded RC specimens. When the rebars were corroded with corrosion degree of 12.8% and 18.9%, the punching shear resistance of L-0 and H-0 decreased by 24.3% and 19.7%, respectively. The is because corrosion decreased the area of steel bars and degraded the bond between concrete and steel bars. The punching shear resistance of L-S-0 and H-S-0 was 5.0% and 2.7% greater than that of L-0 and H-0, respectively. Therefore, adopting the equal-stiffness replacement rule slightly increased the punching shear resistance of the specimens completely reinforced with steel bars. The initial stiffness of L-S-0 and H-S-0 was similar to that of L-0 and H-0, respectively. However, with the increasing displacement, the load resistance of L-S-0 and H-S-0 was greater than that of L-0 and H-0, respectively, under the same displacement. This is because, before yielding of steel bar, the stresses of steel and BFRP bars were similar under the same displacement due to equal-stiffness. However, the stiffness of steel bars significantly decreased once yielding occurred while the stiffness of BFRP did not change.. In this case, the increase of stress of steel bars is much slower than that of BFRP bars. Therefore, the increased load resistance is mainly ascribed to the greater tensile stress of BFRP bars than that of yielded steel bars. However, because the actual corrosion degree was much lower than 20%, the load resistance of L-12.8 was greater than that of L-S-21.1 until the displacement reached 14.1 mm. The punching shear resistance of L-S-21.1 and H-S-22.2 was only 10.0% and 2.4% lower than that of L-0 and H-0, respectively, and was 18.9% and 21.5% higher than that of L-12.8 and H-18.9, respectively. It should be noted that the actual corrosion degrees of L-S-21.1 and H-S-22.2 was higher than that of L-12.8 and H-18.9. Therefore, the effectiveness of the equal-stiffness replacement to resist corrosion should be better under the same corrosion degree, indicating that the hybrid reinforcement under equal-stiffness replacement scheme could effectively moderate the negative effects of rebar corrosion on the punching shear resistance of slab-column connections due to the corrosion-avoidance capacity of the BFRP bars. As shown in **Fig. 10**, steel bar corrosion decreased the deformation capacity of L-0 but increased the deformation capacity of H-0, and so does the energy dissipation capacity which is defined as the area under the load-displacement curve from beginning to failure, as shown in **Table 3**. The hybrid reinforcement with equal-stiffness replacement scheme resulted in both lower deformation capacity and energy dissipation capacity. Moreover, although L-S-21.1 and H-S-22.2 had similar punching shear resistance as L-0 and H-0, the deformation capacity and energy dissipation capacity of L-S-21.1 and H-S-22.2 were much lower than that of L-0 and H-0, respectively.

Deflection of Specimens

Fig. 11 shows the deflection shape of Specimens L-0 and L-12.8. At the initial loading stage, the deflection of the slab almost linearly decreased with increasing distance to the column center. However, at the ultimate stage, the deflection of the slab center was increased sharply and nonlinear compared with surrounding measuring positions, demonstrating that punching shear failure occurred. Similar results were measured for other specimens.

Analytical Study

Identification of Failure Mode

Because the strain of the corroded steel bars was difficult to measure, it was necessary to identify the failure mode of the specimens analytically. Therefore, the yield line method was used to determine the nominal flexural strength of the specimens (F_{pre}), and then the flexural strength F_{pre} was compared with the measured punching shear resistance to judge the failure mode of specimens. As illustrated in **Fig. 12**, only positive yield lines were assumed because the specimens were simply supported. The assumed positive yield lines consist of the yield lines developed along the column edges and the radial yield lines within the polar axis. To simplify the calculation, the rectangular positive yield lines along the column edges were converted to circular positive yield lines with the same perimeter. In this context, the rotation of the circular fan was consistent. Moreover, the rectangular hybrid bar zone and corroded zone in the slab center were converted to circular zones with identical areas. Based on the virtual work principle, **Eqs. 5a** to **5d** were obtained for L-0&H-0, L-12.8&H-18.9, L-S-0&H-S-0, and L-S-21.1&H-S-22.2, respectively, for a given displacement δ

$$F_{\mathrm{Pre}}\delta=\begin{cases}(2\pi r_1 m_{\mathrm{u}}+2\pi(R-r_1)m_{\mathrm{u}})\dfrac{\delta}{R-r_1}, & \text{(5a)}\\[2ex] (2\pi r_1 m_{\mathrm{u,c}}+2\pi(r_2-r_1)m_{\mathrm{u,c}}+2\pi(R-r_2)m_{\mathrm{u}})\dfrac{\delta}{R-r_1}, & \text{(5b)}\\[2ex] (2\pi r_1 m_{\mathrm{u,h}}+2\pi(r_2-r_1)m_{\mathrm{u,h}}+4\alpha(R-r_2)m_{\mathrm{u}}+(2\pi-4\alpha)(R-r_2)m_{\mathrm{u,h}})\dfrac{\delta}{R-r_1}, & \text{(5c)}\\[2ex] (2\pi r_1 m_{\mathrm{u,h,c}}+2\pi(r_2-r_1)m_{\mathrm{u,h,c}}+4\alpha(R-r_2)m_{\mathrm{u}}+(2\pi-4\alpha)(R-r_2)m_{\mathrm{u,h}})\dfrac{\delta}{R-r_1}, & \text{(5d)}\end{cases}$$

where F_{pre} is the virtual load; r_1 and r_2 are the radii of the converted circle, as illustrated in **Fig. 12**; m_{u}, $m_{\mathrm{u,c}}$, $m_{\mathrm{u,h}}$, and $m_{\mathrm{u,h,c}}$ are the nominal flexure strength of slab with uncorroded steel bars, slab with corroded steel bars, slab with uncorroded hybrid bars, and slab with corroded hybrid bars, respectively; α is the angle of the four corners of L-S- and H-S-series specimens with steel bars only, as the parts highlighted by yellow in **Fig. 12b**, which was assumed to be 30° (0.52 rad).

Based on the works of Park and Paulay (2000) and Wight and MacGregor (2011), the nominal flexure strength per unit width of the slab can be calculated by **Eq. 6**

$$\begin{cases} m_{\mathrm{u}} = \rho f_{\mathrm{y}} d^2 (1 - 0.59 \rho f_{\mathrm{y}} / f_{\mathrm{c}}) \\ m_{\mathrm{u,c}} = \rho_{\mathrm{c}} f_{\mathrm{y,c}} d^2 (1 - 0.59 \rho_{\mathrm{c}} f_{\mathrm{y,c}} / f_{\mathrm{c}}) \\ m_{\mathrm{u,h}} = \rho_{\mathrm{h}} f_{\mathrm{yh}} d^2 (1 - 0.59 \rho_{\mathrm{h}} f_{\mathrm{yh}} / f_{\mathrm{c}}) \\ m_{\mathrm{u,h,c}} = \rho_{\mathrm{h,c}} f_{\mathrm{yh,c}} d^2 (1 - 0.59 \rho_{\mathrm{h,c}} f_{\mathrm{yh,c}} / f_{\mathrm{c}}) \end{cases} \tag{6}$$

where ρ, ρ_{c}, ρ_{h}, and $\rho_{\mathrm{e,c}}$ is the tension steel bar ratio, corroded tension steel bar ratio, equivalent tension bar ratio, and equivalent corroded tension bar ratio, respectively; f_{y}, $f_{\mathrm{y,c}}$, f_{yh}, and $f_{\mathrm{yh,c}}$ is the yield strength of uncorroded steel bar, corroded steel bar, equivalent yield strength of the hybrid bar, and equivalent yield strength of the corroded hybrid bar, respectively, $f_{\mathrm{y,c}}$ is calculated based on the suggestion of Weng et al. (2023); d is the effective section depth; f_{c} is the cylinder compressive strength of concrete.

$$\begin{cases} \rho_{\mathrm{c}} = \rho \left(1 - w / 100\right) \\ \rho_{\mathrm{h}} = \rho_{\mathrm{b}} E_{\mathrm{b}} / E_{\mathrm{s}} + \rho \\ \rho_{\mathrm{h,c}} = \rho_{\mathrm{b}} E_{\mathrm{b}} / E_{\mathrm{s}} + \rho_{\mathrm{c}} \end{cases} \tag{7}$$

$$\begin{cases} f_{\mathrm{y,c}} = f_{\mathrm{y}} \left(1 - 1.24 \left(w / 100\right)\right) \\ f_{\mathrm{yh}} = \left(f_{\mathrm{yb}} \rho_{\mathrm{b}} E_{\mathrm{b}} / E_{\mathrm{s}} + f_{\mathrm{y}} \rho \right) / \rho_{\mathrm{h}} \\ f_{\mathrm{yh,c}} = \left(f_{\mathrm{yb}} \rho_{\mathrm{b}} E_{\mathrm{b}} / E_{\mathrm{s}} + f_{\mathrm{y,c}} \rho_{\mathrm{c}} \right) / \rho_{\mathrm{h,c}} \end{cases} \tag{8}$$

where E_{s} and E_{b} indicate the elastic modulus of steel bars and BFRP bars, respectively.

Table 3 lists the calculated F_{pre}. It was found that the ratio of the measured punching shear resistance to the predicted flexural resistance ($V_{\mathrm{u}}/F_{\mathrm{pre}}$) of L-0, L-12.8, L-S-0, L-S-21.1, H-0, H-18.9, H-S-0, and H-S-22.2 was 1.04, 0.90, 0.71, 0.65, 0.83, 0.80, 0.58, and 0.58, respectively. The $V_{\mathrm{u}}/F_{\mathrm{p}}$ of L-0 was greater than 1.0, indicating that this specimen reached its nominal flexural strength before punching shear. In other words, the failure mode of L-0 was flexure-punching shear failure while the rest of specimens failed by pure punching shear failure. This can be proved by the strain gauge results, as shown in **Fig. 13**. The strains of steel bars in the slab center were much greater than that of steel bars in the slab edge, and yielding of steel bars occurred in all specimens except H-S-0. As shown in **Fig. 13a**, for L-0, the strains of steel bar at monitor points SX2 to SX3 yielded, and the strain of steel bar at SX4 reached 1564 με. In comparison, as shown in **Fig. 13(b** to **d)**, the strain of steel bar at SX3 of H-0, L-S-0, and H-S-0 did not yield and the strain of steel bar at SX4 was quite small.

Comparison of Test Results with the Predictions of Code Equations

The measured punching shear resistance of the specimens was compared with the design formula from Chinese code, American code, model code, and European code to evaluate the accuracy of these codes to predict the punching shear resistance of slab-column connections with corroded steel bars, hybrid bars, and corroded hybrid bars. Notable that the Chinese code, American code, and model code define the critical sections as at a distance $d/2$ from the column edges while the European code defines the critical section as the section with $2d$ away from the column edges.

Chinese Code

According to the Chinese code, GB 50010 (2015), the punching shear resistance V_{GB} of the critical section can be calculated with **Eq. 9**.

$$V_{\mathrm{GB}} \leq 0.7\beta_{\mathrm{h}} f_{\mathrm{t}} \eta u_{\mathrm{m}} d \tag{9}$$

$$\eta = \min\left\{0.4 + \frac{1.2}{\beta_{\mathrm{s}}}, 0.5 + \frac{\alpha_{\mathrm{s}} d}{4u_{\mathrm{m}}}\right\} \tag{10}$$

where β_{h} is a factor associated with slab thickness, 1.0 for slab thickness $h \leq 800$ mm and 0.9 for $h \geq 2{,}000$ mm; f_{t} is the axial tensile strength of concrete; u_m is the critical shear perimeter; h_0 is the effective slab depth; β_{s} is the aspect ratio the column section (≥1); and α_{s} is a factor associated with column position, take 40, 30, and 20 for interior, edge, and corner column, respectively.

American Code

Based on the American Code, ACI 318-19 (2019), the punching shear stress v_{ACI} can be calculated by **Eq. 11**.

$$v_{\mathrm{ACI}} = \min\left\{0.17\left(1+\frac{2}{\beta_{\mathrm{s}}}\right)\lambda_{\mathrm{s}}, 0.083\left(2+\frac{\alpha_s d}{u_{\mathrm{m}}}\right), 0.33\lambda_{\mathrm{s}}\right\}\lambda\sqrt{f_{\mathrm{c}}} \tag{11}$$

λ_s is the size effect factor, $\lambda_{\mathrm{s}} = \sqrt{2/\left(1+0.004\cdot d\right)} \leq 1.0$; λ is the concrete density factor, take 1.0 for normal concrete.

Model Code

The Model Code 2010 (fib 2012) suggests calculating the punching shear resistance V_{fib} by **Eq. 12**.

$$V_{\mathrm{Rd,c}} = k_{\psi}\sqrt{f_{\mathrm{c}}}b_0 d \tag{12}$$

$$k_{\psi} = \frac{1}{1.5+0.9k_{\mathrm{dg}}\psi d} \leq 0.6 \tag{13}$$

where k_{dg} is the aggregate size influence parameter, $k_{\mathrm{dg}} = 32/\left(16+d_{\mathrm{g}}\right) \geq 0.75$ for the maximum aggregate size $d_{\mathrm{g}} < 16$ mm and k_{dg}=1.0 for $d_{\mathrm{g}} \geq 16$ mm; the slab rotation ψ is calculated as:

$$\psi = 1.5\cdot\frac{r_{\mathrm{s}}}{d}\cdot\frac{f_{\mathrm{y}}}{E_{\mathrm{s}}}\cdot\left(\frac{m_{\mathrm{Ed}}}{m_{\mathrm{Rd}}}\right)^{1.5} \tag{14}$$

where r_{s} is the location where the radial bending moment equals zero with respect to the support axis; m_{Ed} is the average moment per unit length in the support strip; m_{Rd} is the average flexural strength per unit length in the support strip. For internal column, m_{Ed} can be calculated as:

$$m_{\mathrm{Ed}} = V_{\mathrm{Ed}}\left(\frac{1}{8}+\frac{\left|e_{u,i}\right|}{2\cdot b_{\mathrm{s}}}\right) \tag{15}$$

where $e_{u,i}$ is the eccentricity of the resultant of shear forces with respect to the centroid of the basic control perimeter; V_{Ed} is the shear force at punching; b_{s} is the width of the support strip, $b_{\mathrm{s}}=1.5\cdot\sqrt{r_{\mathrm{s,x}}\cdot r_{\mathrm{s,y}}}$; m_{Rd} is calculated as

$$m_{\mathrm{Rd}}=\rho\cdot f_{\mathrm{y}}\cdot d^{2}\cdot(1-\frac{\rho\cdot f_{\mathrm{y}}}{2\cdot f_{\mathrm{c}}}) \tag{16}$$

European Code

As suggested by the European code, Eurocode 2 (CEN 2004), the punching shear stress v_{CNE} of can be calculated by **Eq. 17**.

$$v_{\mathrm{CEN}}=0.18k\left(100\rho_{\mathrm{s}}f_{\mathrm{c}}\right)^{1/3}\geq v_{\min}=0.035k^{3/2}\sqrt{f_{\mathrm{c}}} \tag{17}$$

where k is the factor considering size effect, $k=1+\sqrt{200/d}\leq 2.0$; ρ_{s} is the tension reinforcement ratio, $\rho=\sqrt{\rho_{x}\rho_{y}}\leq 0.02$.

Comparison of Calculated Load Resistance with Test Results

The predicted punching shear resistance according to the above code equations is summarized in **Table 4** and **Fig. 14**. The average ratio of the measured value to the predicted value was 0.99, 0.97, 1.34, and 1.06 for GB 50010 (2015), ACI 318 (ACI 2019), Eurocode 2 (CEN 2004), and Model code (fib 2012), respectively. Therefore, GB 50010 (2015), ACI 318 (ACI 2019), and Model code (fib 2012) could well predict the punching shear resistance of the specimens while the predictions of Eurocode 2 (CEN 2004) were conservative. It is worthwhile noting that the standard deviation (SD) and coefficient of variation (CV) of GB 50010 (2015) and ACI 318 (ACI 2019) were large, i.e., 0.23 for both. This was ascribed to the exclusion of the contribution of reinforcement and therefore, the effects of variation of reinforcement could not be considerred. If only focus on specimens with corroded steel bars, the average ratio of the measured value to the predicted value was 0.82, 0.79, 1.17, and 0.84 for GB 50010 (2015), ACI 318 (ACI 2019), Eurocode 2 (CEN 2004), and Model code (fib 2012), respectively. In addition, if only focus on specimens with hybrid corroded steel bars and BFRP bars, the average ratio of the measured value to the predicted value was 0.98, 0.97, 1.32, and 1.15 for GB 50010 (2015), ACI 318 (ACI 2019), Eurocode 2 (CEN 2004), and Model code (fib 2012), respectively. Therefore, only Eurocode 2 (CEN 2004) produced safe predictions for specimens with corrosion although it is conservative. As shown in **Fig. 14**, generally, the calculated results were located in the domain with a maximum error of 35%. All the predicted results of Eurocode 2 (CEN 2004) were lower than the measured ones regardless of corrosion of steel bars is considered or not.

Punching Shear Resistance - Critical Shear Crack Theory

The critical shear crack theory (CSCT) proposed by Muttoni (2008) was also adopted here to calculate the punching shear resistance of uncorroded slab-column connections, and the modified CSCT modified by Qian et al. (2022a) was used to predict the punching shear resistance of corroded slab-column connections. In the CSCT, both the load-rotation relationship and the failure criteria are required to judge the ultimate stage of the slab-column connections, the punching shear resistance V_R is obtained at the intersection of the two curves, as shown in **Fig. 15**.

Load-Rotation Relationship

As suggested by Muttoni (2008), the load-rotation relationship of slab-column connections without shear reinforcement can be defined by **Eq. 18**

$$V = \frac{2\pi}{r_q - r_c} \cdot \begin{pmatrix} -m_r \cdot r_0 + m_R \cdot \langle r_y - r_0 \rangle + EI_1 \cdot \psi \cdot \langle \ln(r_1) - \ln(r_y) \rangle + \\ EI_1 \cdot \chi_{TS} \cdot \langle r_1 - r_y \rangle + m_{cr} \cdot \langle r_{cr} - r_1 \rangle + EI_0 \cdot \psi \cdot \langle \ln(r_s) - \ln(r_{cr}) \rangle \end{pmatrix} \tag{18}$$

The meaning of the parameters in **Eq. 18** and the corresponding calculated method can be found in Muttoni (2008), which is not presented herein for the sake of brief.

Failure Criteria

The semi-empirical failure criterion proposed by Muttoni (2008) is shown in **Eq. 19**, which was modified by Qian et al. (2022a) to account for the effects of corrosion by introducing a factor *k* associated with corrosion degree *w*, as shown in **Eq. 20**.

$$\frac{V_{\mathrm{R}}}{b_0 d\sqrt{f_c^{'}}} = \frac{3/4}{1+15\dfrac{k\psi d}{d_{g0}+d_g}} \tag{19}$$

$$k = \begin{cases} 1, & \text{for} \quad w=0 \\ e^{0.016w}, & \text{for } 0 \le w \le 30\% \end{cases} \tag{20}$$

where V_{R} is the punching shear resistance; b_{o} is the control shear perimeter with $d/2$ from the column edge; d_{go} is a referential size equal to 16 mm; and d_g is the maximum aggregate size; ψ is rotation of slab.

Fig. 16 compares the predicted punching shear resistance of the CSCT with measured ones, the punching shear resistance of the uncorroded and corroded slab-column connections was well predicted by the CSCT (Muttoni 2008) and modified CSCT (Qian et al. 2022a), respectively. The maximum error was less than 10%. Therefore, the CSCT (Muttoni 2008) and modified CSCT (Qian et al. 2022a) were reliable methods to predict the punching shear resistance of uncorroded and corroded slab-column connections, respectively, regardless of hybrid bars were considered or not.

Conclusion

An experimental study of eight large-scale slab-column connections is conducted to investigate the efficiency of partially replacing steel bars by BFRP bars based on equal-stiffness rule to resist corrosion. Moreover, an analytical study is performed to quantitatively identify the failure mode of the specimens and to evaluate the accuracy of the equations of prevalent design codes and the critical shear crack theory to predict the punching shear resistance of slab-column connections. Based on the experimental and analytical studies results, the main conclusions are drawn below:

1. Test results demonstrated that the punching shear resistance of the RC slab-column connections with tension reinforcement ratios of 0.52% and 0.91% decreased by 19.7% to 24.3% under the corrosion degrees of 13.0% and 17.6%, respectively. Following equal-stiffness replacement rule, replacing partial of steel rebar by BFRP bars may increase the load resistance but decrease the deformation capacity and energy dissipation capacity slightly. The corroded composite slab-column connections reinforced by hybrid bars achieved greater load resistance but lower ductility than the corroded RC slab-column connections.
2. Steel bar corrosion decreased the deformation capacity of the slab-column connections with low reinforcement ratio but increased the deformation capacity of the slab-column connection with high reinforcement ratio. The equal-stiffness replacement rule resulted in lower deformation capacity and energy dissipation capacity. In addition, whilst corroded composite slab-column connections reinforced hybrid bars had similar punching shear resistance as uncorroded RC slab-column connections, both the deformation capacity and energy dissipation capacity of corroded composite slab-column connections reinforced hybrid bars were lower than that of uncorroded RC slab-column connections.
3. Analytical work indicated that GB 50010 (2015), ACI 318 (ACI 2019), and Model code (fib 2012) may overestimate the punching shear resistance of corroded specimens. However, Eurocode 2 (CEN 2004) could obtain conservative results regardless of whether corrosion of steel bars was considered. The CSCT (Muttoni 2008) was reliable to predict the punching shear resistance of uncorroded slab-column connections regardless of they were reinforced hybrid bars or not. The modified CSCT (Qian et al.

2022a) was reliable to predict the punching shear resistance of corroded slab-column connections regardless of they were reinforced hybrid bars or not.

Acknowledgments

This research was supported by a research grant provided by the National Natural Science Foundation of China (Nos. U22A20244, 52022024). Any opinions, findings and conclusions expressed in this paper are those of the writers and do not necessarily reflect the view of the National Natural Science Foundation of China.

Data Availability

Some or all data, models, or code that support the findings of this study are available from the corresponding author upon reasonable request.

Reference

American Concrete Institute. 2019. *Building code requirements for structural concrete and commentary*. ACI 318-19. Farmington Hills, MI: ACI.

Aljazaeri, Z., Alghazali, H. H., and Myers, J. J. 2020. "Effectiveness of using carbon fiber grid systems in reinforced two-way concrete slab system." *ACI Structural Journal*, 117(2): 81-89. https://doi.org/10.14359/51720198.

Auyeung, Y., Balaguru, P., and Chung, L. 2000. "Bond behavior of corroded reinforcement bars." *ACI Structural Journal*, 97(2): 214-220. https://doi.org/10.14359/826.

Cairns, J., Plizzari, G. A., Du, Y., Law, D. W., and Franzoni, C. 2005. "Mechanical properties of corrosion-damaged reinforcement." *ACI Materials Journal*, 102(4): 256-264. https://doi.org/10.14359/14619.

CEN (European Commitee for Standardization). 2004. *Design of concrete structures—Part 1-1: General rules and rules for buildings*. Eurocode 2. Brussels, Belgium: CEN.

fib (Fédération International du Béton). 2012. *Model Code 2010*. Bulletins d'Informations 65 and 66. Lusanne, Lusanne, Switzerland: fib.

Hassan, M., Ahmed, E., and Benmokrane, B. 2013a. "Punching-shear strength of normal and high-strength two-way concrete slabs reinforced with GFRP bars." *Journal of Composites for Construction*, 17(6): 04013003. https://doi.org/10.1061/(ASCE)CC.1943-5614.0000424.

Hassan, M., Ahmed, E. A., and Benmokrane, B. 2013b. "Punching shear strength of glass fiber-reinforced polymer reinforced concrete flat slabs." *Canadian Journal of Civil Engineering*, 40(10): 951-960. https://doi.org/10.1139/cjce-2012-0177.

Huang, Z., Zhao, Y., Zhang, J., and Wu, Y. 2020. "Punching shear behaviour of concrete slabs reinforced with CFRP grids." *Structures*, 26: 617-625. https://doi.org/10.1016/j.istruc.2020.04.047.

Long, N. M., and Marián, R. 2013. "Punching shear resistance of interior GFRP reinforced slab-column connections." *Journal of Composites for Construction*, 17(1): 2-13. https://doi.org/10.1061/(ASCE)CC.1943-5614.0000324.

Ministry of Housing and Urban-Rural Development of the People's Republic of China. 2015. *Code for design of concrete structures*. GB 50010-15. Beijing: China, Architecture & Building Press.

Muttoni, A. 2008. "Punching shear strength of reinforced concrete slabs without transverse reinforcement." *ACI Structural Journal*, 105(4): 440-450. https://doi.org/10.14359/19858.

Park, R., and Paulay, T. (2000). "CH4-Strength of Members with Flexure." Reinforced concrete structures, John Wiley & Sons.

Qian, K., Li, J. S., Huang, T., Weng, Y. H., and Deng, X. F. 2022a. "Punching shear strength of corroded reinforced concrete slab-column connections." *Journal of Building Engineering*, 45: 103489. https://doi.org/10.1016/j.jobe.2021.103489.

Qian, K., Liu, J. G., Yu, X. H., and Weng, Y. H. 2022b. "Experimental and numerical investigation of punching shear capacity of corroded reinforced concrete slab-column connections." *Structures*, 43: 1548-1557. https://doi.org/10.1016/j.istruc.2022.07.065.

Said, M. E., and Hussein, A. A. 2019a. "Effect of bandwidth reinforcement corrosion on the response of two way slabs." *Construction and Building Materials*, 216: 137-148. https://doi.org/10.1016/j.conbuildmat.2019.04.034.

Said, M. E., and Hussein, A. A. 2019b. "Structural behavior of two-way slabs with large corroded area." *Engineering Structures*, 199: 109556. https://doi.org/10.1016/j.engstruct.2019.109556.

Sim, C., and Frosch, R. J. 2020. "Cracking behavior of slabs with corrosion-resistant and high-strength reinforcing bars." *ACI Structural Journal*, 117(5): 245-257. https://doi.org/10.14359/51724684.

Weng, Y. H., Fu, F., and Qian, K. 2023. "Punching shear resistance of corroded slab–column connections subjected to eccentric load." *Journal of Structural Engineering*, 149(1): 04022219. https://doi.org/10.1061/(ASCE)st.1943-541x.0003504.

Weng, Y. H., Qian, K., Fu, F., and Fang, Q. 2020. "Numerical investigation on load redistribution capacity of flat slab substructures to resist progressive collapse." *Journal of Building Engineering*, 29: 101109. https://doi.org/10.1016/j.jobe.2019.101109.

Wight, J. K., and MacGregor, J. G. 2011. *Reinforced concrete mechanics and design*, NJ: Prentice-Hall.

Table 1. Specimen details

Specimen	Size (m)	Concrete strength		Slab tension reinforcement				Corrosion degree	
		f_c (MPa)	f_t (MPa)	Reinforced scheme	ρ_s (%)	ρ_b (%)	P_h (%)	Target (%)	Measured (%)
L-0		43.7	3.0	Steel bar	0.52	\	0.52	\	/
L-12.8		45.6	3.1	Steel bar	0.52	\	0.52	20	12.8
L-S-0		42.0	3.1	Hybrid bar	0.26	1.04	0.52	\	/
L-S-21.1	2.2×2.2×0.15	40.5	3.0	Hybrid bar	0.26	1.04	0.52	20	21.1
H-0		36.3	2.7	Steel bar	0.91	\	0.91	\	/
H-18.9		41.1	2.9	Steel bar	0.91	\	0.91	20	18.9
H-S-0		41.9	3.0	Hybrid bar	0.46	1.84	0.91	\	/
H-S-22.2		41.5	3.0	Hybrid bar	0.46	1.84	0.91	20	22.2

Note: f_c and f_t denote cylinder compressive strength and tensile strength of concrete, respectively; ρ_s, ρ_b, and ρ_h indicate steel bar ratio, BFRP bar ratio, and hybrid bar ratio, respectively. The ρ_h is obtained by converting BFRP bar to steel bar of the same stiffness.

Table 2 Material test results

Item	Diameter (mm)	Elastic modulus (MPa)	Yield strength (MPa)	Tensile strength (MPa)	Elongation (%)
Steel bar	10	216,000	567	717	15.0
	12	201,000	532	695	22.1
BFRP bar	12	47,000		1257	2.7
	17	48,000		1337	2.9

Table 3 Test results

Specimens	Critical loads (kN)			V_u / F_{pre}	R_s	Dissipated energy (kN·mm)	Failure mode
	V_{cr}	V_u	F_{pre}				
L-0	101	280	270	1.04	3.3d	6,670	FP
L-12.8	/	212	238	0.90	3.7d	3,889	P
L-S-0	107	294	412	0.71	4.4d	3,544	P
L-S-21.1	/	252	387	0.65	7.3d	5,278	P
H-0	128	376	452	0.83	2.6d	3,102	P
H-18.9	/	302	380	0.80	3.4d	5,096	P
H-S-0	135	386	670	0.58	4.3d	2,614	P
H-S-22.2	/	367	631	0.58	7.3d	3,043	P

Note: V_{cr} and V_u denote cracking strength and punching shear strength, respectively; F_{pre} indicates predicted norminal flexural strength; FP and P indicate flexure-punching failure and punching shear failure, respectively; d is the effective section depth.

Table 4 Comparison of calculated load resistance with measured ones

Specimen ID	GB 50010		ACI 318		Eurocode 2		Model Code	
	V_{GB} (kN)	$\frac{V_u}{V_{GB}}$	V_{ACI} (kN)	$\frac{V_u}{V_{ACI}}$	V_{CEN} (kN)	$\frac{V_u}{V_{CEN}}$	V_{fib} (kN)	$\frac{V_u}{V_{fib}}$
L-0	315	0.89	327	0.86	210	1.33	295	0.95
L-20	326	0.65	334	0.63	203	1.05	285	0.74
L-S-0	320	0.92	321	0.92	221	1.33	248	1.19
L-S-20	315	0.80	315	0.80	209	1.21	233	1.08
H-0	284	1.33	298	1.26	238	1.58	334	1.13
H-20	305	0.99	318	0.95	232	1.30	326	0.93
H-S-0	318	1.21	321	1.20	261	1.48	313	1.23
H-S-20	315	1.16	319	1.15	257	1.43	299	1.23
Mean		0.99		0.97		1.34		1.06
SD		0.23		0.22		0.17		0.17
CV		0.23		0.22		0.12		0.16

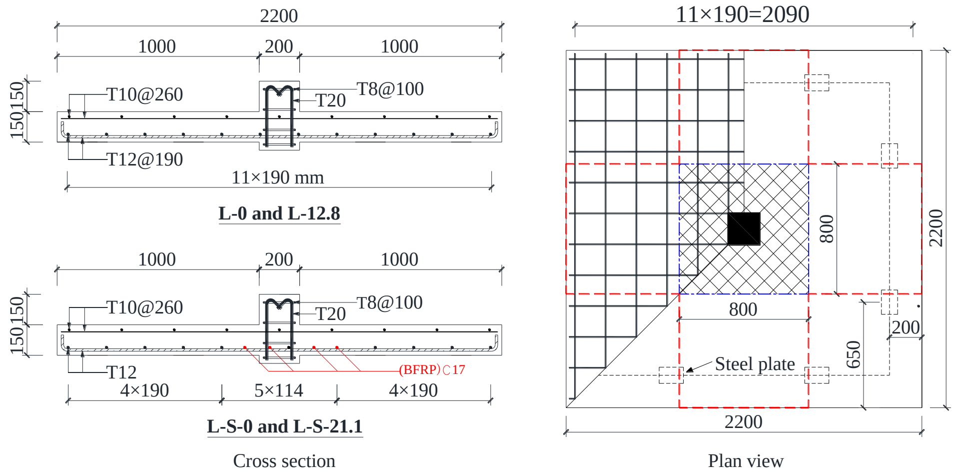

(a)

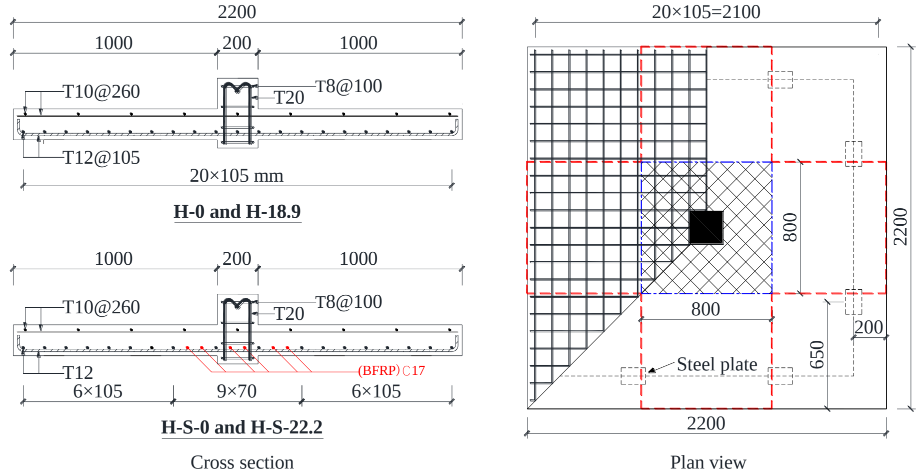

(b)

Fig. 1 Details of the specimens: (a) specimens with slab tension reinforcement ratio of 0.52%; (b) specimens with slab tension reinforcement ratio of 0.91% (the zone enveloped by the red dashed line is reinforced with hybrid bars, if any)

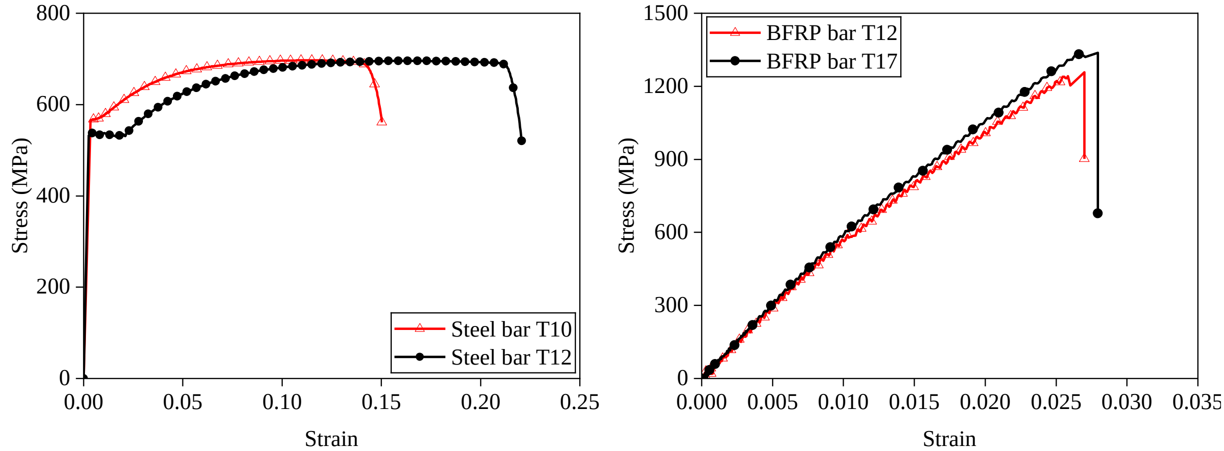

Fig. 2 Tensile stress-strain curve of steel bars and bars

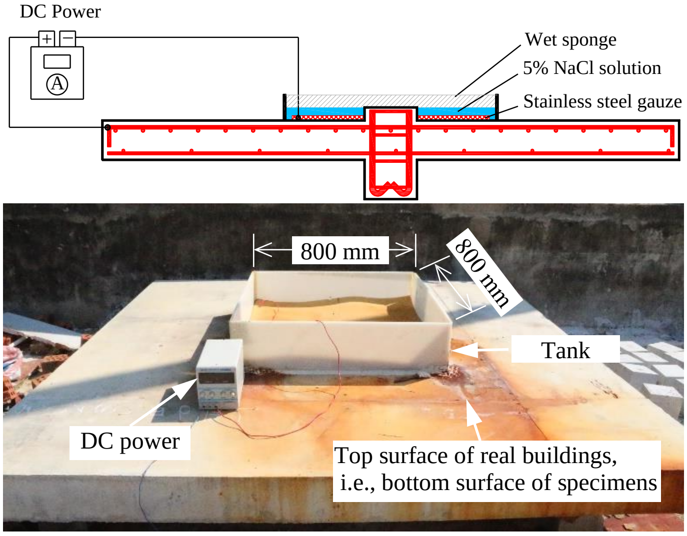

Fig. 3 Setup of electrified accelerated corrosion

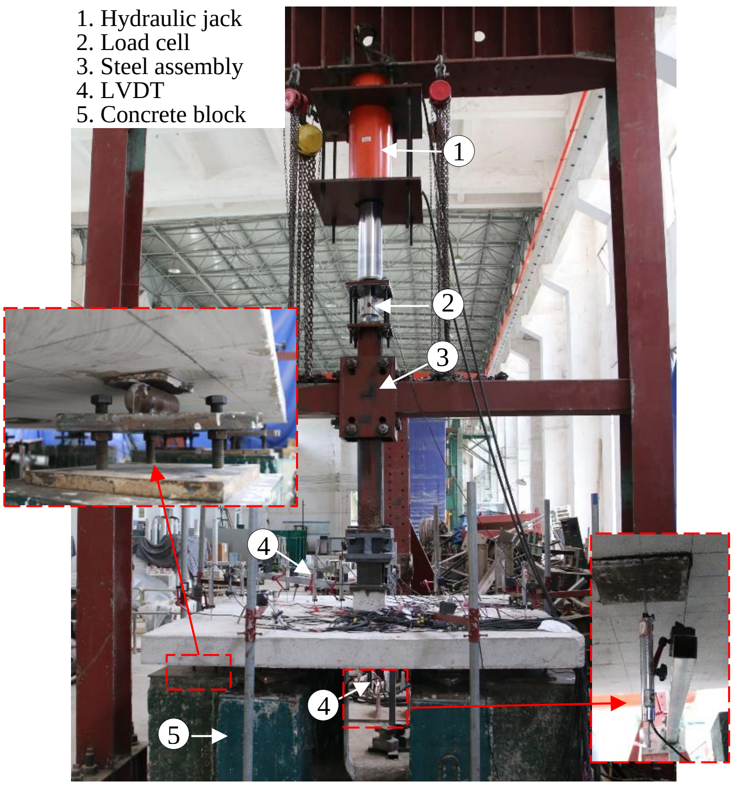

Fig. 4 Test setup

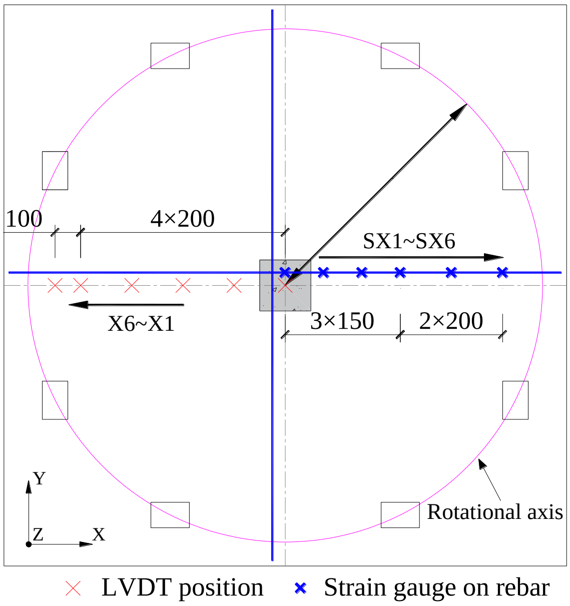

Fig. 5 Layout of LVDTs and strain gauges

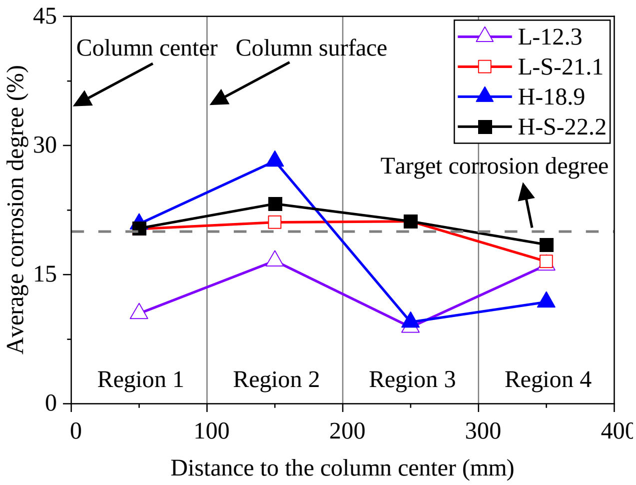

Fig. 6 Corrosion degree distribution

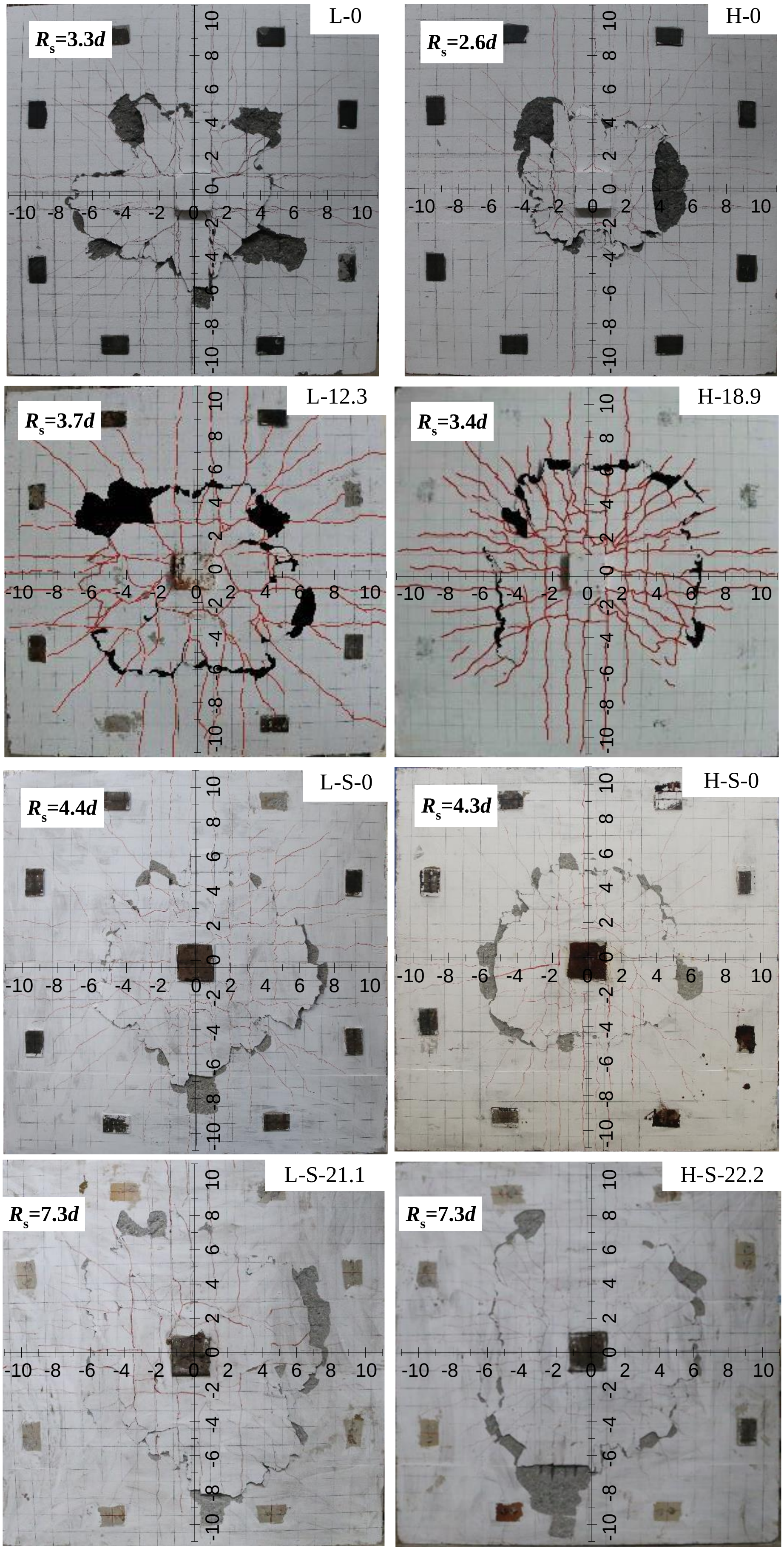

Fig. 7 Crack patterns and failure modes of the specimens (unit in decimeter)

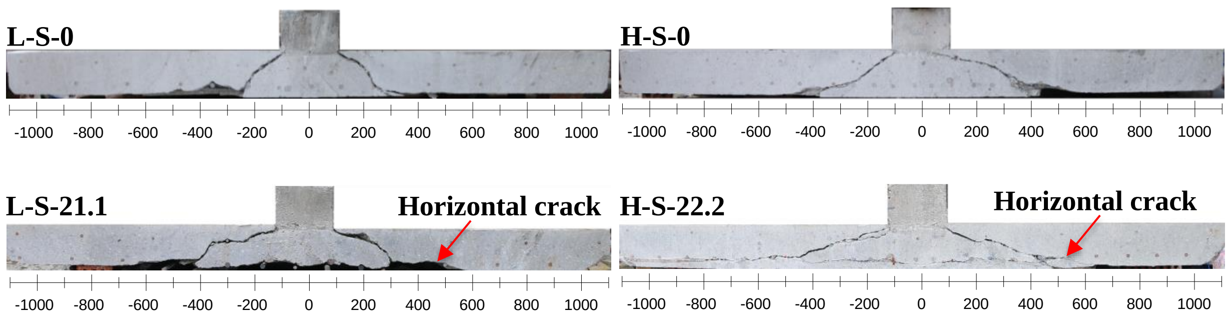

Fig. 8 Punching shear cone of the specimens (unit in mm)

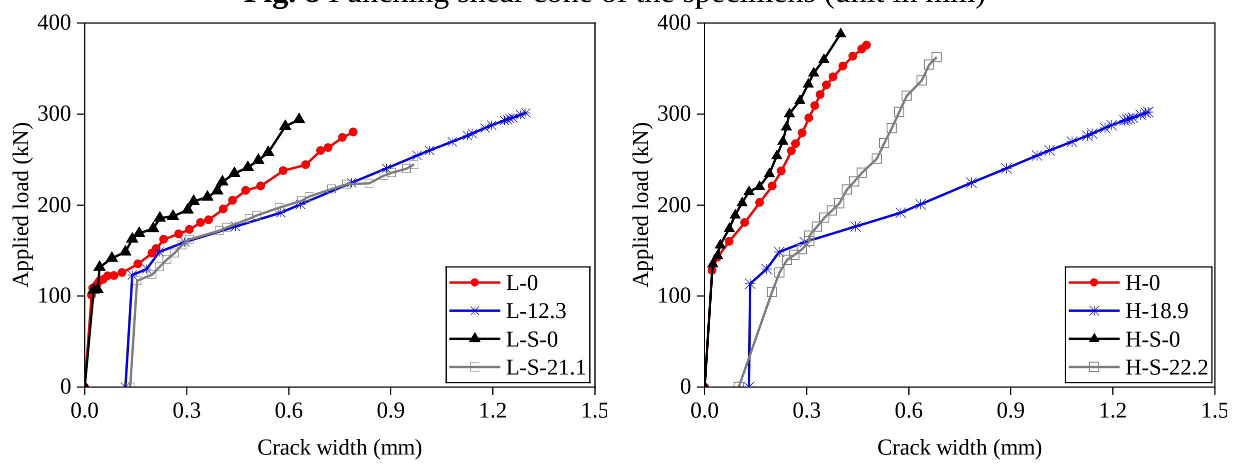

(a) (b)

Fig. 9 Relationship between crack width and applied load: (a) specimens with low tension reinforcement ratio; (b) specimens with high tension reinforcement ratio

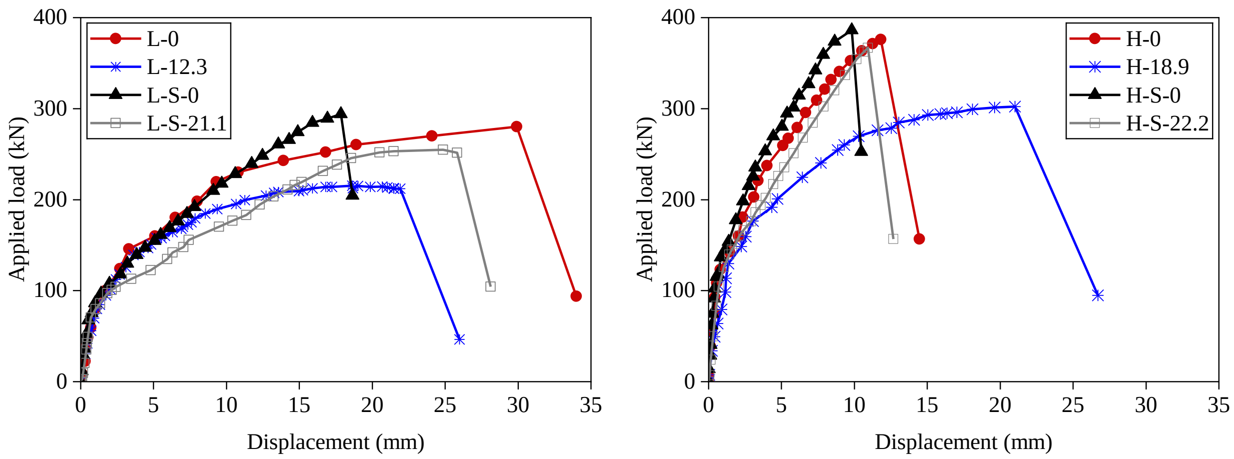

(a) (b)

Fig. 10 Load-displacement curves: (a) specimens with a tension reinforcement ratio of 0.52%; (b) specimens with a tension reinforcement ratio of 0.91%

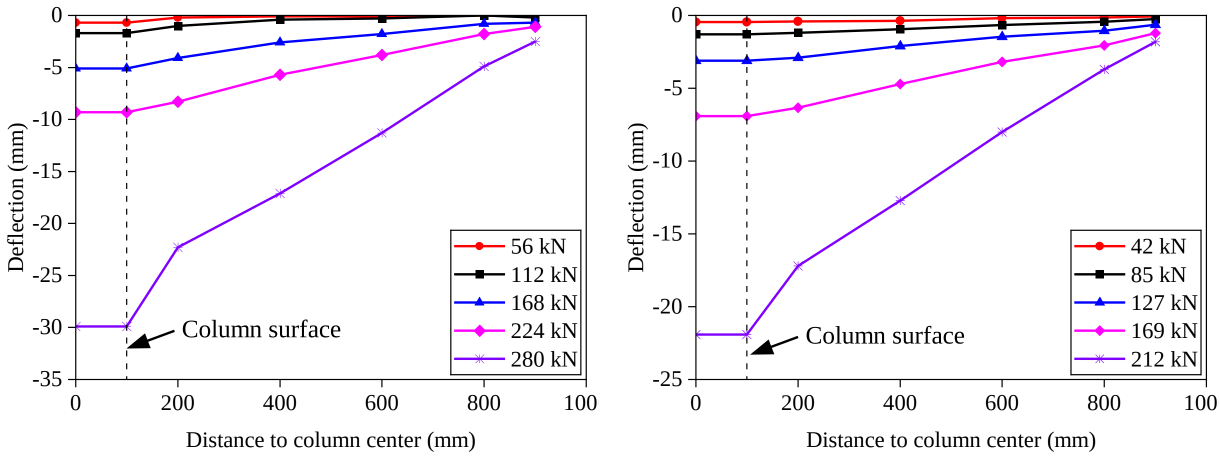

(a) (b)

Fig. 11 Deflection of specimens: (a) L-0; (b) L-12.8

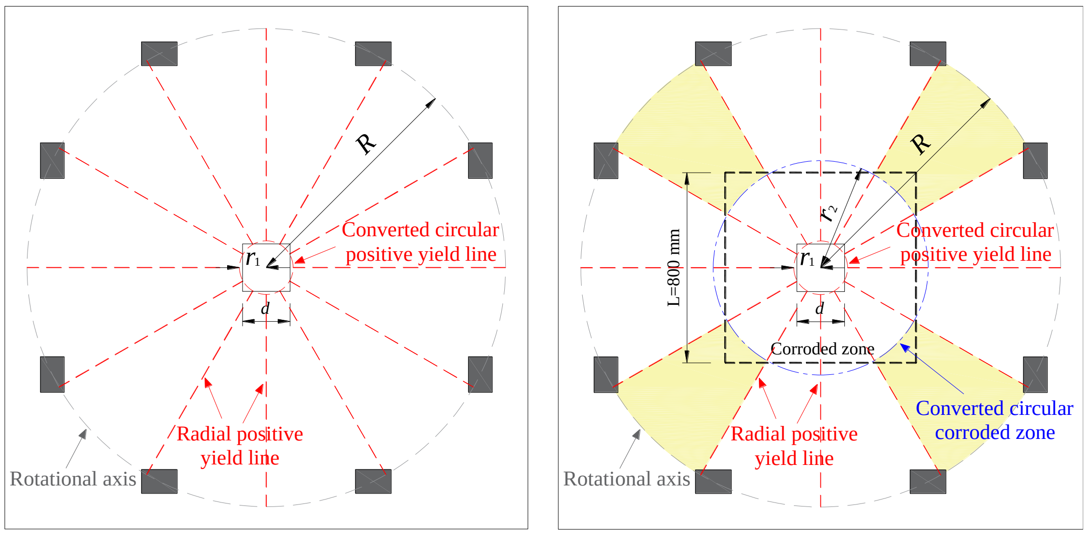

(a) (b)

Fig. 12 Assumed yield line pattern: (a) RC specimens; (b) corroded RC specimens and specimens with hybrid bars

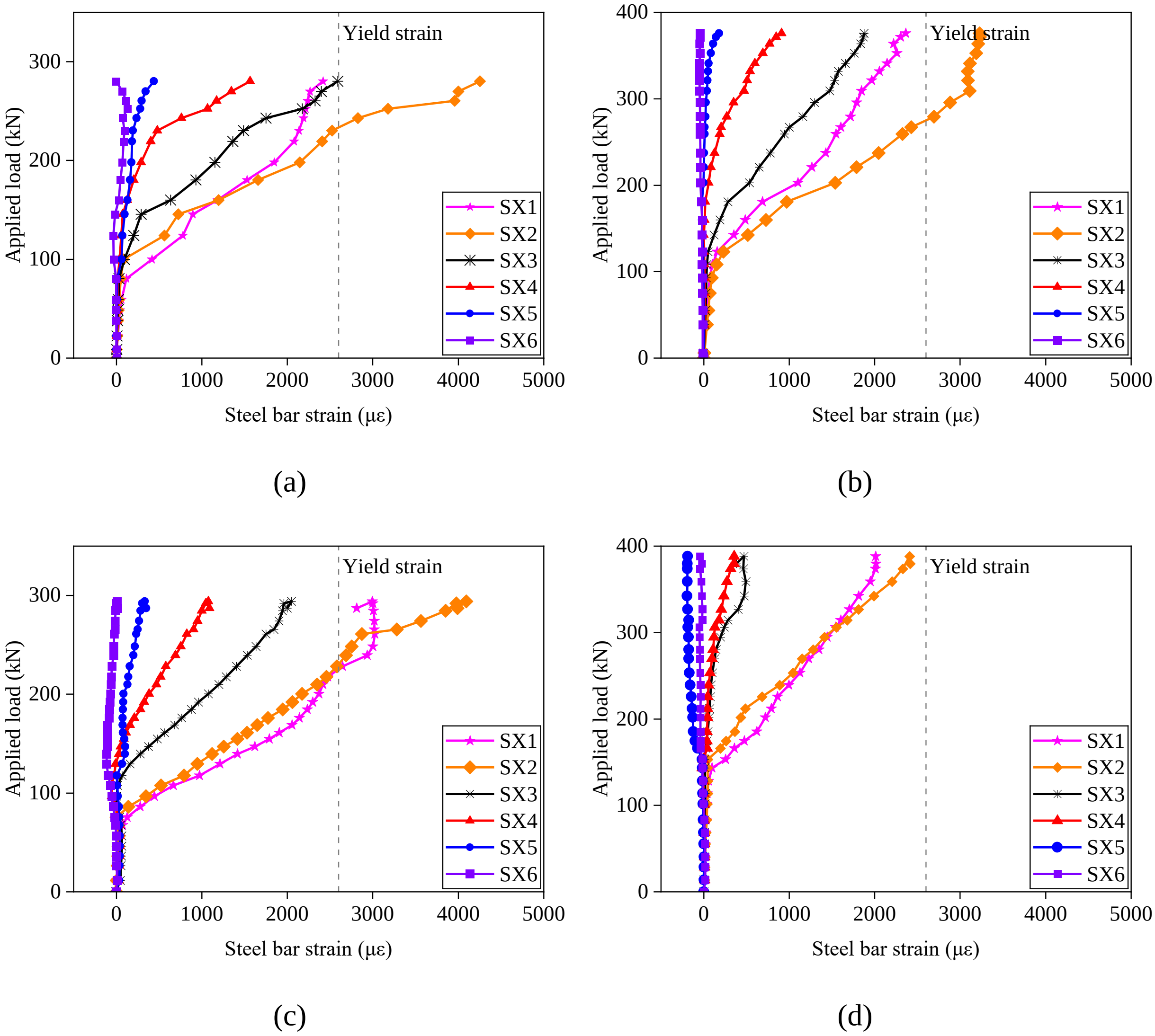

Fig. 13 Strain of steel bar: (a) L-0; (b) H-0; (c) L-S-0; (d) H-S-0

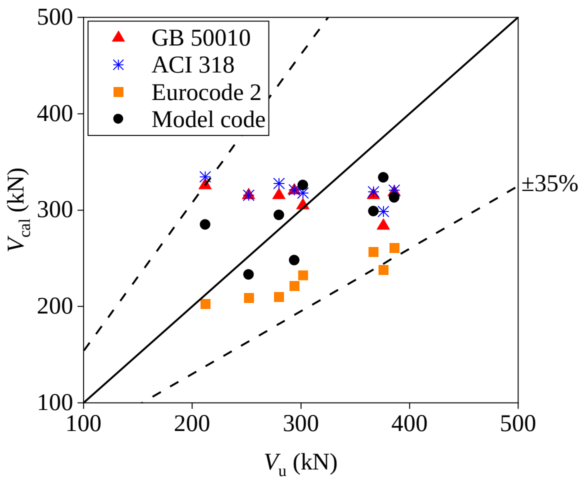

Fig. 14 Comparison of calculated punching shear strength of code equations with measured ones

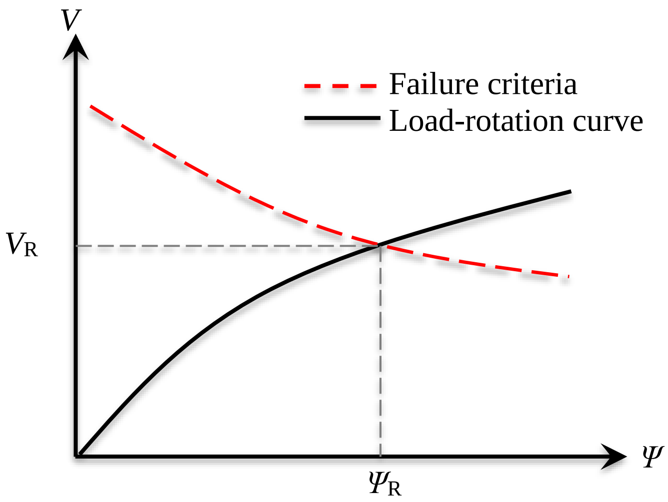

Fig. 15 Load-rotation relationship and failure criteria of the CSCT

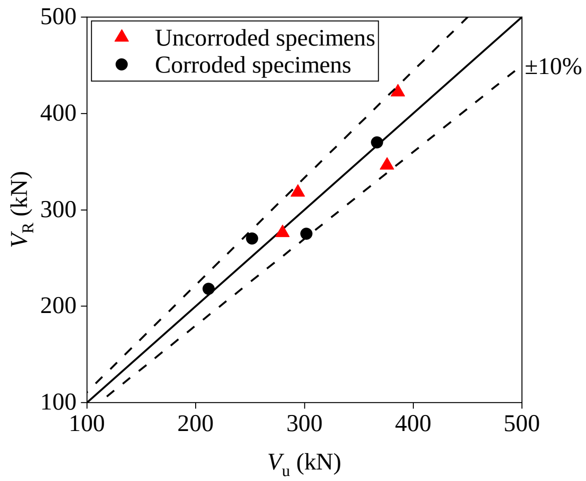

Fig. 16 Comparison of predicted punching shear strength of the CSCT with measured ones